Supplementary Material

Using machine-learned force fields for describing heat-transport related quantities in AlGaN and derived materials

Simon Fernbach, Egbert Zojer and Natalia Bedoya-Martínez

1 Moment Tensor Potentials

A detailed description of moment-tensor potentials is provided in the original paper by Shapeev et al. [1]. In the following, their fundamental character shall be summarized briefly. Moment tensor potentials (MTPs) are interatomic potentials that use moment tensors as basis functions to expand the potential energy [2][1]. These are tensor products of the relative positions of an atom and its neighbors. They are local in the sense that the total potential energy can be expanded as a sum of contributions from individual atoms

$$E_{\mathbf{pot}} = \sum_{\mathbf{i}} V(\eta_i)$$

where η_i is called the neighborhood of atom i. It consists of a set of properties for all atoms j in some neighborhood of the atom defined by a cutoff radius $R_{\mathbf{cut}}$. The properties are the relative position $\vec{r}_{ij} = \vec{r}_i - \vec{r}_j$, type of the central atom z_i, and the type of neighbor atoms z_j. Thus η_i is a set given by

$$\eta_i = \{ (\vec{r}_{i1}, z_i, z_1), \ldots, (\vec{r}_{iM}, z_i, z_M), R_{\mathbf{cut}} \}$$

where M is the number of atoms in the neighborhood. The energy contributions of individual atoms can be expanded as

$$V(\eta_i) = \sum_{\alpha=1}^{N_B} \xi_\alpha B_\alpha$$

where ξ_α are parameters, B_α moment tensor basis functions and N_B the number of MTP basis functions, with both to be defined further below. The fundamental building blocks of these basis functions B_α are the so-called moment tensors defined as

$$\mathrm{M}_{\mu,\nu}(\eta_i) = \sum_j f_\mu(|r_{ij}|, z_i, z_j) \underbrace{\boldsymbol{r}_{ij} \otimes \ldots \otimes \boldsymbol{r}_{ij}}_{\nu \textbf{ times}}$$

, they consist of an angular part given by the ν-fold tensor product of relative positions, a radial part $f_\mu(|\vec{r}_{ij}|, z_i, z_j)$ and the sum runs over all neighboring atoms. The radial part is given by

$$f_\mu(|r_{ij}|, z_i, z_j) = \sum_{\beta=1}^{N_Q} c^\beta_{\mu,z_i,z_j} Q^\beta(|\boldsymbol{r}_{ij}|)$$

$$Q^\beta(|\boldsymbol{r}_{ij}|) = \begin{cases} \varphi^\beta(|\boldsymbol{r}_{ij}|)(R_{cut} - |\boldsymbol{r}_{ij}|)^2 & |\boldsymbol{r}_{ij}| < R_{cut} \\ 0 & |\boldsymbol{r}_{ij}| > R_{cut} \end{cases}$$

. Here, $Q^\beta(\vec{r}_{ij})$ are radial basis functions, with $\varphi^\beta(|\vec{r}_{ij}|)$ polynomial functions (e.g Chebyshev polynomials) and c^β_{μ,z_i,z_j} radial parameters; N_Q is the number of used radial basis functions, which can be freely chosen and is independent of the level of the MTP. The descriptors $M_{\mu,\nu}(\eta_i)$ are tensors of rank ν and because the actual basis functions are scalar, they need to be suitably contracted. Some examples of contractions resulting in scalars are

$$\mathrm{M}_{0,1} \cdot \mathrm{M}_{1,1}, \qquad \mathrm{M}_{1,2} : \mathrm{M}_{0,2}, \qquad \mathrm{M}_{0,1} \cdot \mathrm{M}_{0,1} M_{0,0}$$

Any such scalar contraction is a valid moment tensor basis function B_α. In the following, we drop the contraction symbols and always imply a correct contraction of products of MTP descriptors. Since there are infinitely many basis functions, a suitable way to restrict the basis set is needed. To achieve this, one defines the level of an MTP descriptor as

$$\mathrm{lev}\mathrm{M}_{\mu\nu} = 2 + 4\mu + 2\nu$$

The level of a basis function is simply defined as the sum of the levels of descriptors involved in the contraction e.g: $\mathrm{lev}(\mathrm{M}_{1,1}\mathrm{M}_{0,2})\mathrm{M}_{0,1} = 18$ or $\mathrm{lev}\mathrm{M}_{1,2}\mathrm{M}_{0,2} = 16$. The level of a particular MTP is now defined as the maximum level $\mathbf{lev_{max}}$ of basis functions B_α included in the basis set. This effectively limits the basis set to a finite number of basis functions N_B containing only moment tensors with levels smaller or equal to the desired MTP level. Further details can be found in [3][4].

2 Error trends as a function of training hyperparameters

Here we report the influence of various training-related hyperparameters, such as the MTP level, the number of configurations in the training dataset, and the magnitude of atomic displacements in the training data on various physical observables. The respective training datasets are described in Section 2.2 of the main text. To assess fluctuations arising from the random initialization of MTP parameters during training, we construct ensembles of MTPs and evaluate the errors between the predictions of individual ensemble members and DFT. The ensemble mean and standard deviation of these errors provide a more robust measure for assessing the impact of training-related hyperparameters on the resulting MTPs. These quantities are shown as solid and dotted red lines.

In Figure S3, which compares the errors of MTPs trained on datasets with larger (Section 2.2, set 1) and smaller (Section 2.2, set 2) atomic displacements, it should be noted that the significantly larger errors in forces, stresses, and energies for the MTPs trained on the dataset with larger displacements most likely arise from the correspondingly more distorted validation configurations. These configurations are inherently more challenging, making accurate predictions of forces, stresses, and energies more difficult.

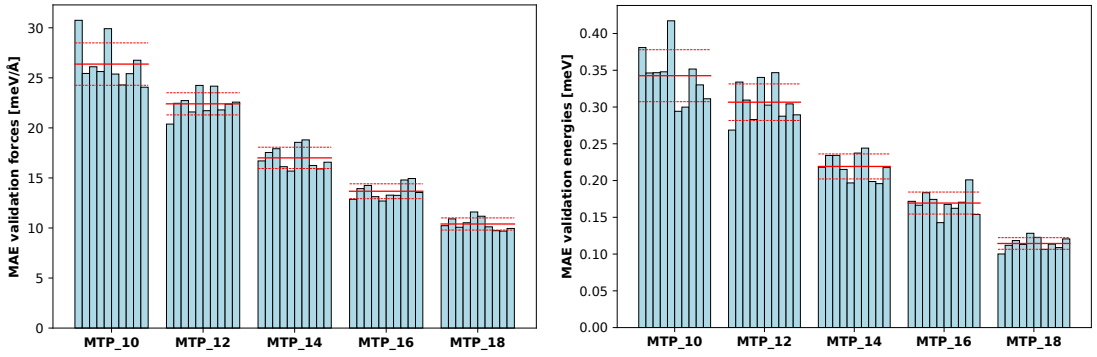

(a) **Validation forces**

(b) **Validation energies**

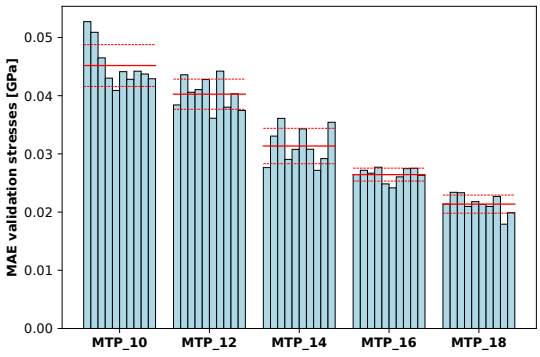

(c) **Validation stresses**

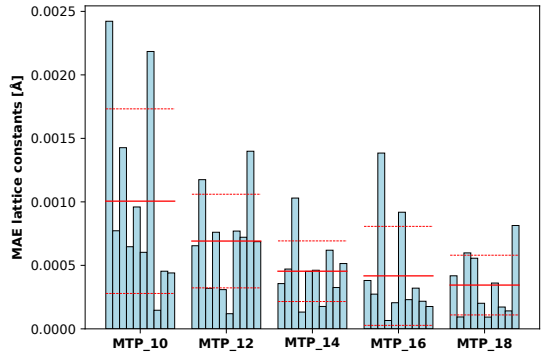

(d) **Lattice constants**

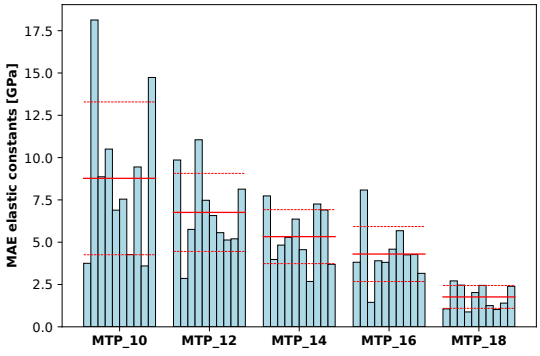

(e) **Elastic constants**

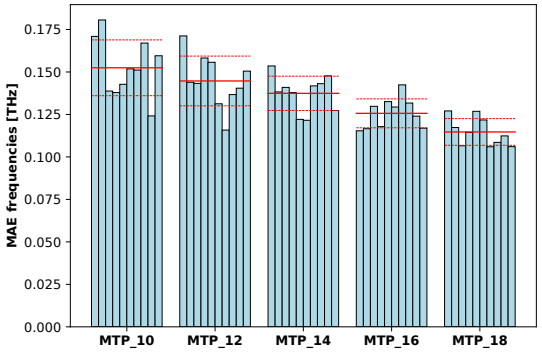

(f) **Phonon frequencies**

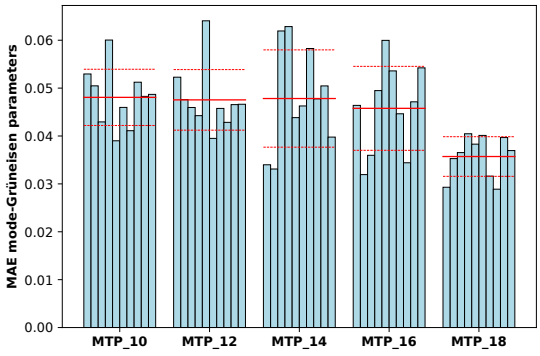

(g) **Mode-Grüneisen parameters**

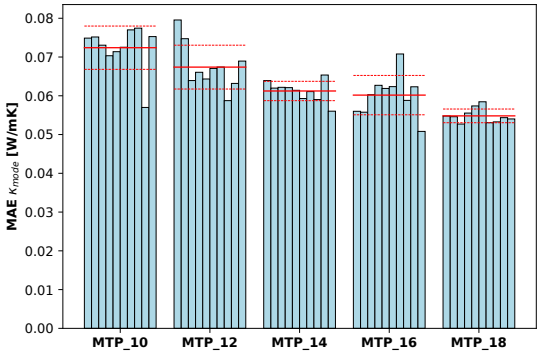

(h) **Mode-thermal conductivities**

Figure S1: Mean absolute errors of validation forces, stresses and energies, lattice and elastic constants, phonon frequenies (on a irr. BZ mesh), mode-Grüneisen parameters and mode-thermal conductivities. The mean absolute errors are calculated as the mean values of differences between the results of ten independently parametrized MTPs at various MTP levels and DFT-calculated reference data. MTP levels considered are 10, 12, 14, 16 and 18. The MTP are all trained using the same 300 configurations from the main dataset (Section 2.2, set 1).

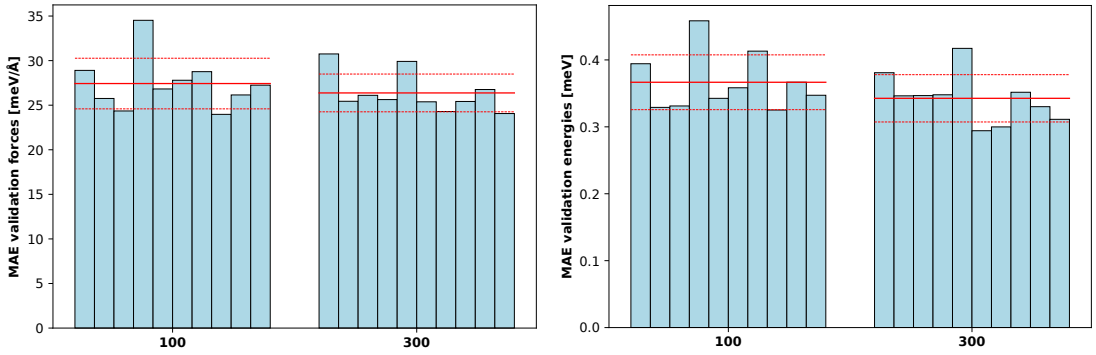

(a) **Validation forces**

(b) **Validation energies**

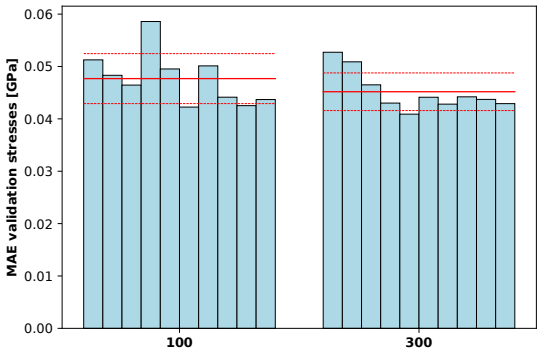

(c) **Validation stresses**

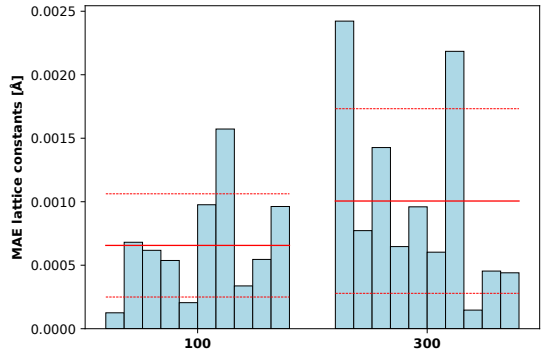

(d) **Lattice constants**

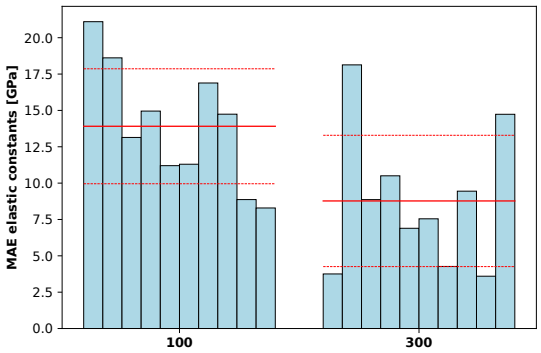

(e) **Elastic constants**

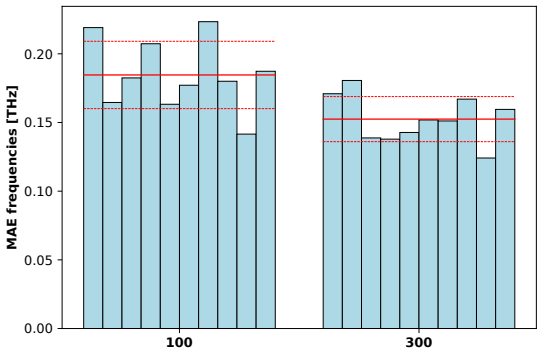

(f) **Phonon frequencies**

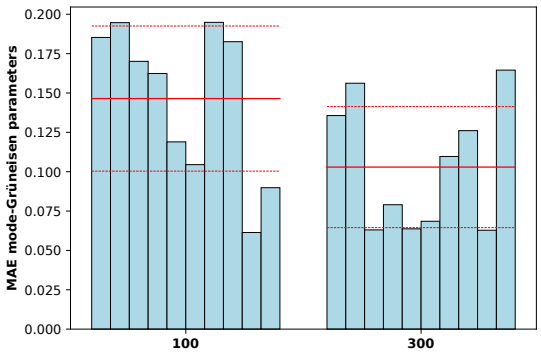

(g) **Mode-Grüneisen parameters**

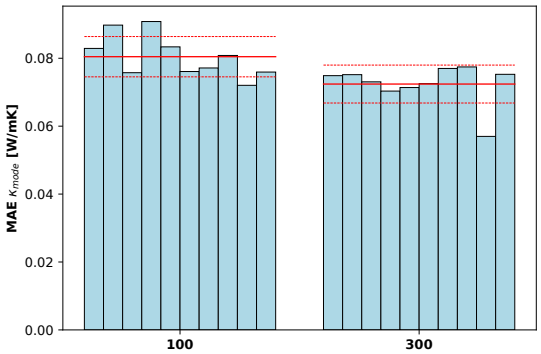

(h) **Mode-thermal conductivities**

Figure S2: Mean absolute errors of validation forces, stresses and energies, lattice and elastic constants, phonon frequenies (on a irr. BZ mesh), mode-Grüneisen parameters and mode-thermal conductivities. The mean absolute errors are calculated as the mean values of differences between the results of ten independently parametrized level-10 MTPs trained on 100 and 300 configurations from the main training dataset (Section 2.2, set 1) respectively and the DFT-calculated reference data.

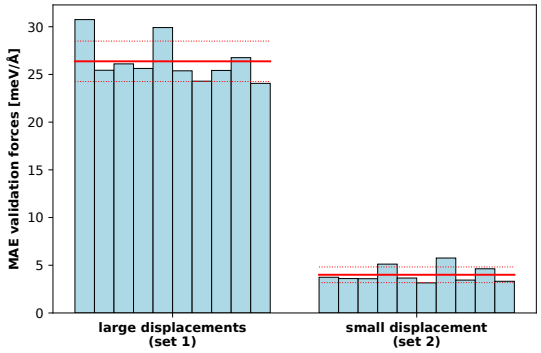

(a) **Validation forces**

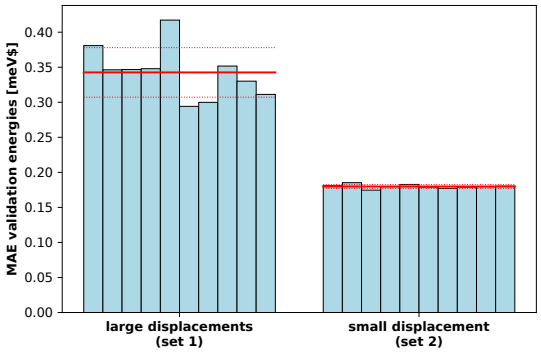

(b) **Validation energies**

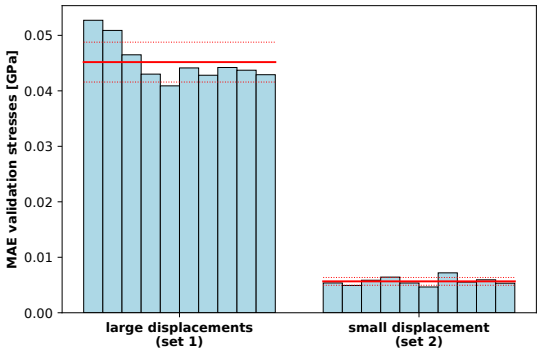

(c) **Validation stresses**

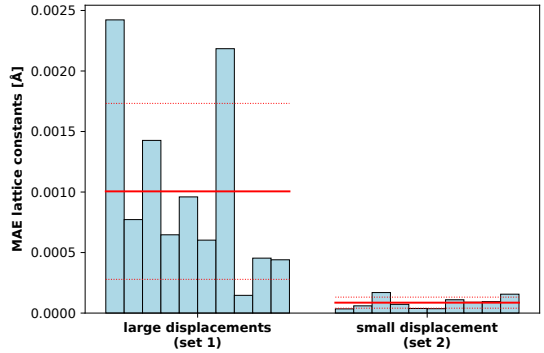

(d) **Lattice constants**

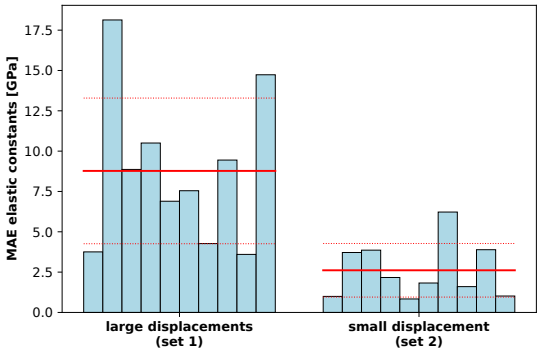

(e) **Elastic constants**

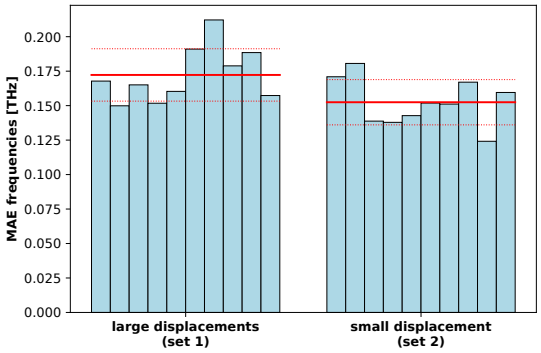

(f) **Phonon frequencies**

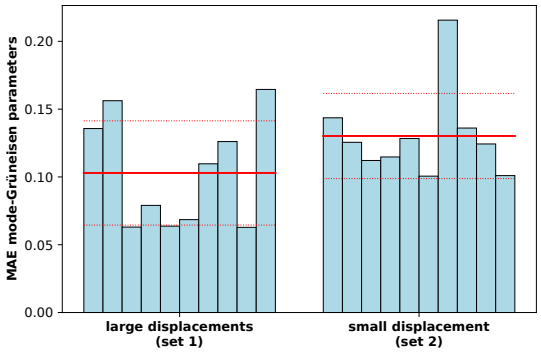

(g) **Mode-Grüneisen parameters**

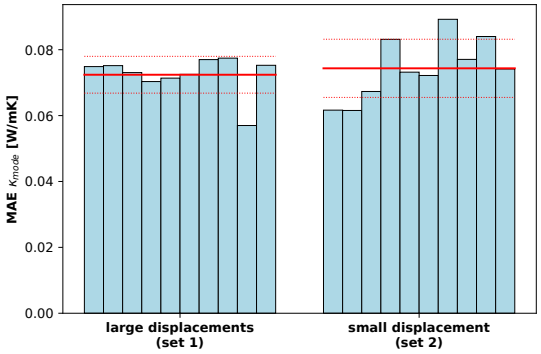

(h) **Mode-thermal conductivities**

Figure S3: Mean absolute errors of validation forces, stresses and energies, lattice and elastic constants, phonon frequenies (on a irr. BZ mesh), mode-Grüneisen parameters and mode-thermal conductivities. The mean absolute errors are calculated as the mean values of differences between the results of ten independently parametrized level-10 MTPs trained on a dataset containing larger atomic displacements (Section 2.2, set 1) and one with smaller displacements (Section 2.2, set 2) and reference data calculated with DFT.

3 Elastic constants

Table S1: Overview of available experimental data for the elastic constants of wurtzite AlN and GaN at room temperature, with values in GPa. Errors are shown in brackets where available. For AlN, McNeil [5] measured a bulk single crystal using Brillouin zone scattering; Sotnikov [6] reported a bulk single-crystalline sample using surface acoustic wave (SAW) measurements; Deger [7] measured a thin film using SAW; Kim measured a bulk single crystal using the resonance method; Ohashi [8] measured a bulk single crystal using ultrasonic microscopy. For GaN, Polian [9] and Deguchi [10] measured bulk single crystals using Brillouin zone scattering; Yamaguchi [11] measured a single-crystalline thin film using Brillouin zone scattering; Takagi [12] measured a thin film of unknown crystal quality using Brillouin zone scattering; Deger [7] measured a single-crystalline thin film using SAW. Units are in GPa.

	AlN					**GaN**				
	McNeil [5]	Sotnikov [6]	Deger [7]	Kim [13]	Ohashi [8]	Takagi [12]	Yamaguchi [11]	Polian [9]	Deger [7]	Deguchi [10]
C_{11}	410.5(10)	402.5(0.5)	410	412.6(0.5)	401.2(0.5)	374	365	390(15)	370	373
C_{33}	388.5(10)	387.6(1)	390	386.1(4.5)	368.2(27.9)	379	381	398(20)	390	387
C_{44}	124.6(4.5)	122.9(0.5)	120	127.4(0.9)	122.6(0.2)	101	109	105(10)	90	93.6
C_{12}	148.5(10)	135.6(0.5)	140	126.6(0.5)	135(0.5)	106	135	145(20)	145	141
C_{13}	98.9(3.5)	101(2)	100	118.8(0.9)	96.3(22.1)	70	114	106(20)	110	80.4

4 Phonon frequencies

Table S2: Overview of experimentally determined Raman frequencies from the literature for wurtzite AlN and GaN, reported in wavenumbers [cm^{-1}]. All measurements were performed at room temperature.

	AlN						GaN					
ν [cm^{-1}]	Jin [14]	Hayes [15]	Kuball [16]	McNeil [5]	Davydov [17]	Haboeck [18]	Kuball [16]	Kozawa [19]	Manchon [20]	Perlin [21]	Davydov [17]	Callsen [22]
E2(low)	248	-	-	252	249	249	144	-	145	144	144	145
A1(TO)	610	613	610	614	611	610	532	534	533	531	532	534
E2(high)	656	659	656	660	657	656	567	572	568	568	568	569
E1(TO)	670	672	669	673	671	669	559	563	559	560	559	560
A1(LO)	-	893	890	893	890	891	734	736	-	-	734	736
E1 (LO)	913	915	911	916	912	912	741	745	-	-	741	741

Table S3: Results for the Raman frequencies of wurtzite AlN and GaN. Presented are DFT-calculated values, results from the material-specific MTPs (MTP), and results from the alloy MTP (MTP_{alloy}), along with the range of experimental values compiled from Table S2. Experimental data were measured at $T = 300$ K, while all calculated results are at 0 K.

	AlN				GaN			
	DFT	MTP	MTP_{alloy}	Exp	DFT	MTP	MTP_{alloy}	Exp.
E2(low)	236	234	234	248[14]–252[5]	138	142	144	144[16] – 145[22]
A1(TO)	610	606	608	610[14]–614[5]	525	525	532	531[21]–534[22]
E2(high)	656	656	655	656[14]–660[5]	556	557	561	567[16]–572[19]
E1(TO)	667	672	658	669[16]–673[5]	548	548	545	559[16]–563[19]
A1(LO)	875	873	874	890[16]–893[5]	716	716	721	734[16]–736[19]
E1 (LO)	900	904	893	911[16]–916[5]	721	721	719	741[16]–745[19]

5 Mode-Grüneisen parameters

Table S4: Overview of the available experimental data for the mode-Grüneisen parameters of Raman-active modes in wurtzite AlN and GaN. All experimental values are measured at room temperature.

	AlN					GaN			
ν [cm^{-1}]	Goni [23]	Kuball [16]	Van Uden [24]	Li [25]	Manjón [26]	Goni [23]	Siegle [27]	Callsen [22]	Perlin [21]
E2(low)	0.1(5)	-	-	-	0.06	-0.4(1)	-	-0.43	-
A1(TO)	1.51(5)	1.39	1.30(1)	1.10	1.49	1.47(4)	1.51(4)	1.52	1.18
E2(high)	1.58(1)	1.71	1.62(2)	1.43	1.72	1.50(1)	1.50(1)	1.46	1.80
E1(TO)	1.41(1)	1.57	1.42(2)	-	1.66	1.41(1)	1.41(1)	1.55	1.61
A1(LO)	-	0.93	1.02(1)	0.96	0.86	1.20(5)	1.20(3)	1.24	-
E1(LO)	1.06(3)	1.26	1.04(4)	-	1.09	-	-	1.29	-

Table S5: Comparison between simulations and experimets for the Grüneisen parameters of Raman-active modes in wurtzite AlN and GaN. Given are DFT-calculated values, results obtained with the material-specific MTPs and the alloy MTP, and the range of experimental values determined from Table S4. Experimental data were measured at $T = 300$ K, while calculated results are at $T = 0$ K.

	AlN				GaN			
	DFT	MTP	MTP$_{\text{alloy}}$	Exp	DFT	MTP	MTP$_{\text{alloy}}$	Exp.
E2(low)	-0.1	-0.1	-0.54	0.06[26]–0.1[23]	-0.32	-0.1	-0.24	-0.43[22] – -0.40[23]
A1(TO)	1.41	1.37	1.44	1.10[25]–1.51[23]	1.60	1.54	1.79	1.18[21]–1.52[22]
E2(high)	1.67	1.67	1.53	1.43[25]–1.72[26]	1.60	1.61	1.62	1.46[22]–1.80[21]
E1(TO)	1.50	1.46	1.47	1.41[23]–1.66[26]	1.49	1.39	1.68	1.41[23]–1.61[21]
A1(LO)	1.03	1.10	1.13	0.93[16]–1.02[24]	1.22	1.33	1.47	1.20[23]–1.24[22]
E1(LO)	1.12	1.18	1.18	1.04[24]–1.26[16]	1.21	1.30	1.47	1.29[22]

6 DFT convergence tests

To establish that our DFT results are reliable, we performed a series of convergence tests for the wavefunction cutoff (`ecutwfc`) and the electronic reciprocal grid size (`k-grid`). These tests are discussed below. We begin with the most basic and also most important quantities for this work: the forces, stresses, and energies in our training data.

To verify convergence, two random configurations were selected from the main dataset (Section 2.2) and evaluated using different DFT parameter settings. Since these configurations correspond to highly deformed supercells with large atomic displacements, the convergence tests applied here are stricter than those typically used for equilibrium structures, where convergence is generally achieved more readily. If the mean relative errors across all Cartesian force components, stress tensor components, and energies in both supercells fall below their respective thresholds, the calculations are considered converged. For consistency, the stresses are multiplied by the supercell volume to obtain virial stresses in units of energy. The convergence thresholds are set to 1 meV/Å for forces and 1 meV/atom for both stresses and energies [28, 29]. The results of these tests are shown in Figure S4, where the red lines depict the convergence thresholds and the red crosses indicate the DFT parameters used in this work. We use a wavefunction cutoff of 90 Ry (1225 eV), which is converged for AlN and almost converged for GaN, with the energy slightly above the threshold. Due to the high computational cost of further increasing the cutoff, this was not deemed feasible. For the reciprocal grid size, we chose $4 \times 4 \times 4$, which is converged for both AlN and GaN.

In addition to forces, stresses, and energies, we also checked key material properties such as the lattice constants, elastic constants, and the Gamma-point phonon frequencies. The results are shown in Figure S5. The cutoffs and reciprocal grid sizes used in this work are indicated by red dashed lines. We use a cutoff of 90 Ry (1250 eV) for both AlN and GaN, and a reciprocal grid size of $10 \times 10 \times 10$. As shown, all properties are well converged for both materials.

Lastly, for thermal transport, we tested the convergence of the thermal conductivity with respect to the supercell size used for the third-order force constants (Figure S6) and the size of the reciprocal phonon sampling grid (Figure S7). The difference between a $2 \times 2 \times 2$ and a $2 \times 2 \times 3$ supercell is negligible, so we use a $2 \times 2 \times 2$ cell. For thermal conductivity calculations that only involve three-phonon processes, we use a phonon grid of $20 \times 20 \times 20$, which is sufficient for the benchmarking performed in this work. The change relative to a much larger grid ($32 \times 32 \times 32$) is less than 5%. For calculations involving four-phonon processes, performed only for GaN, the computational cost grows rapidly with grid size. However, we find that the difference between an $11 \times 11 \times 11$ and a $12 \times 12 \times 12$ grid is less than 2%, so we use a $12 \times 12 \times 12$ reciprocal phonon grid.

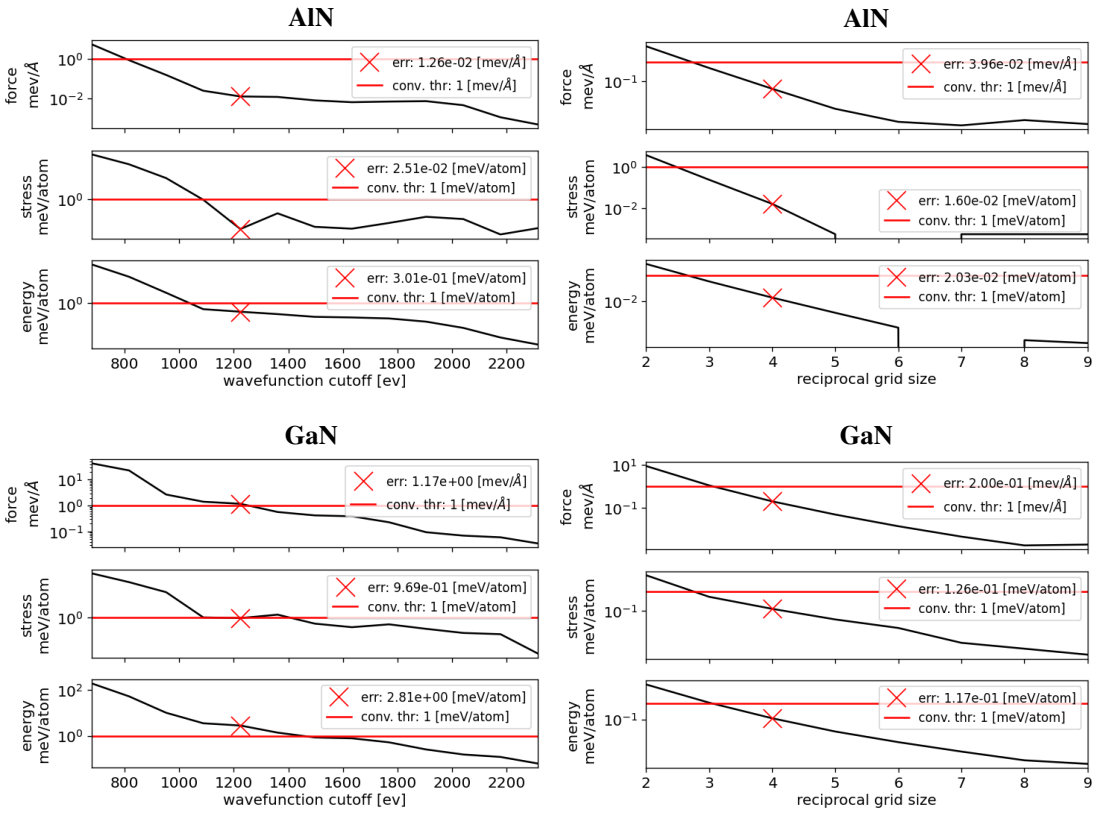

Figure S4: The changes in the mean absolute errors of forces, stresses, and energies are shown as a function of the wavefunction cutoff (left panels) and the electron reciprocal-space grid size (right panels). As a reference, results obtained with a maximum wavefunction cutoff of 180 Ry (2450 eV) and a maximum reciprocal grid size of $10 \times 10 \times 10$ are used.

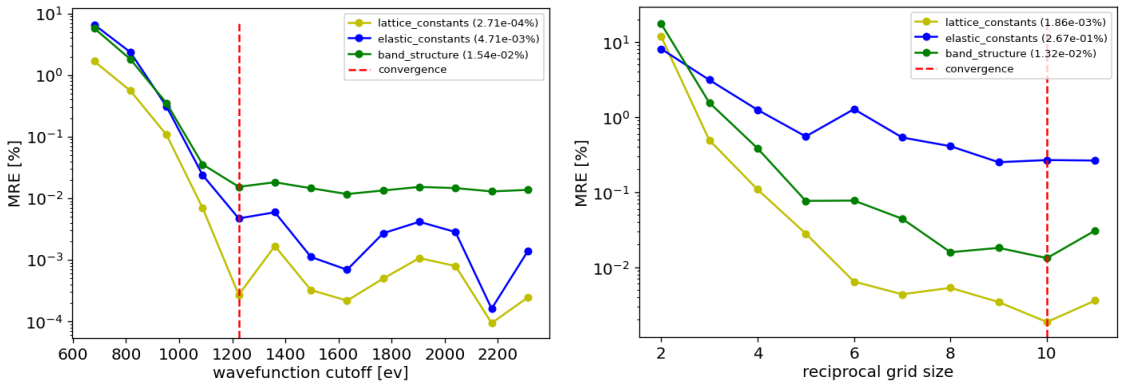

(a) **AlN** (b) **AlN**

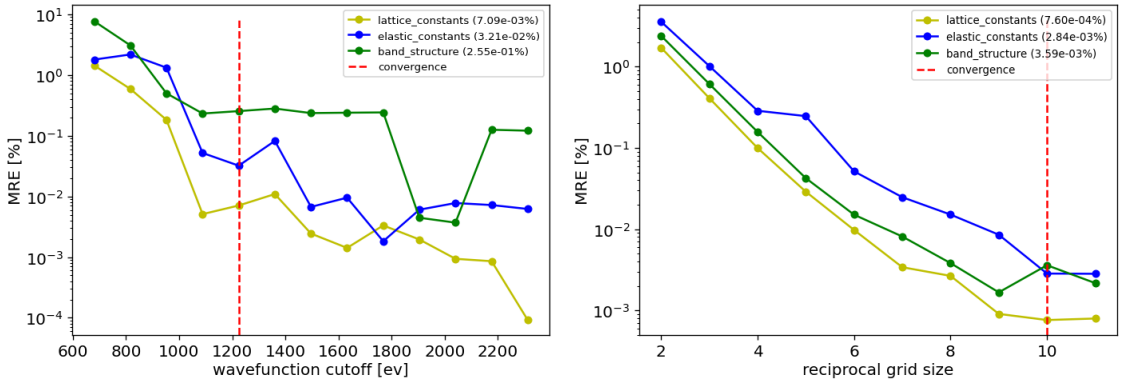

(c) **GaN** (d) **GaN**

Figure S5: Change in the mean relative errors of DFT-calculated lattice constants, elastic constants, and phonon frequencies (on a BZ grid) for AlN (top row) and GaN (bottom row) as a function of the wavefunction cutoff (left column) and the reciprocal-space grid size (right column). The changes are determined relative to a maximum cutoff of 180 Ry (2450 eV) and a maximum reciprocal grid size of $12 \times 12 \times 12$. The red dashed line indicates the values beyond which convergence is achieved.

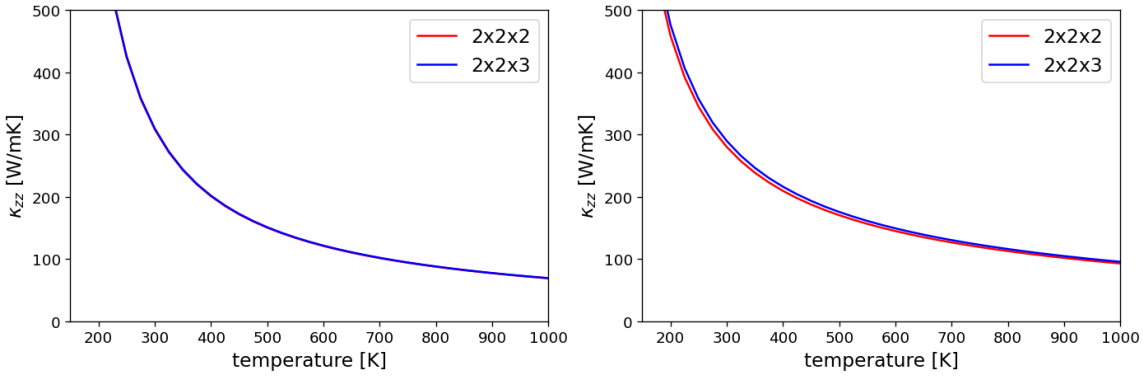

(a) AlN (b) GaN

Figure S6: Comparison of DFT-calculated κ_{zz} (RTA) obtained using 2×2×2 (red) and 2×2×3 (blue) supercells for the calculation of third-order force constants. Results for AlN are shown on the left, and results for GaN on the right. In this work, we use the 2×2×2 supercell.

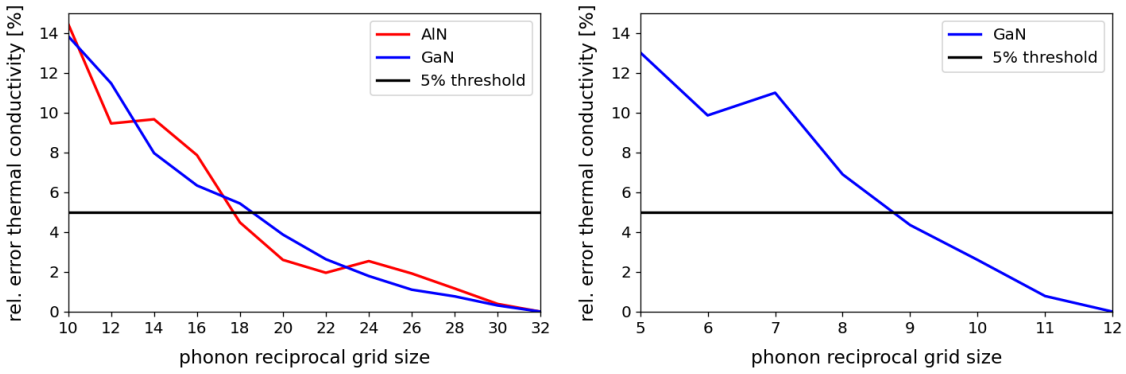

(a) 3ph

(b) 3ph+4ph

Figure S7: Convergence of the average thermal conductivity at 300 K, calculated with ShengBTE in the RTA, as a function of the reciprocal-space phonon grid size. The left panel shows results including only three-phonon scattering, while the right panel includes both three- and four-phonon scattering processes. In this work, we use a $20 \times 20 \times 20$ grid for three-phonon calculations and a $12 \times 12 \times 12$ grid for four-phonon calculations.

References

[1] A. V. Shapeev, "Moment Tensor Potentials: A Class of Systematically Improvable Interatomic Potentials," *Multiscale Modeling & Simulation*, vol. 14, no. 3, pp. 1153–1173, 2016. [Online]. Available: https://doi.org/10.1137/15M1054183

[2] I. S. Novikov, K. Gubaev, E. V. Podryabinkin, and A. V. Shapeev, "The MLIP package: moment tensor potentials with MPI and active learning," *Machine Learning: Science and Technology*, vol. 2, no. 2, p. 025002, dec 2020. [Online]. Available: https://dx.doi.org/10.1088/2632-2153/abc9fe

[3] A. V. Shapeev, "Moment Tensor Potentials: A Class of Systematically Improvable Interatomic Potentials," *Multiscale Modeling & Simulation*, vol. 14, no. 3, pp. 1153–1173, 2016. [Online]. Available: https://doi.org/10.1137/15M1054183

[4] K. Gubaev, E. Podryabinkin, and A. Shapeev, "Machine learning of molecular properties: Locality and active learning," *The Journal of Chemical Physics*, vol. 148, 09 2017.

[5] L. E. McNeil, M. Grimsditch, and R. H. French, "Vibrational Spectroscopy of Aluminum Nitride," *Journal of the American Ceramic Society*, vol. 76, no. 5, pp. 1132–1136, 1993. [Online]. Available: https://ceramics.onlinelibrary.wiley.com/doi/abs/10.1111/j.1151-2916.1993.tb03730.x

[6] A. Sotnikov, H. Schmidt, M. Weihnacht, E. Smirnova, T. Chemekova, and Y. Makarov, "Elastic and Piezoelectric Properties of AlN and LiAlO2 Single Crystals," *Ultrasonics, Ferroelectrics and Frequency Control, IEEE Transactions on*, vol. 57, pp. 808 – 811, 05 2010.

[7] C. Deger, E. Born, H. Angerer, O. Ambacher, M. Stutzmann, J. Hornsteiner, E. Riha, and G. Fischerauer, "Sound velocity of $Al_xGa_{1-x}N$ thin films obtained by surface acoustic-wave measurements," *Applied Physics Letters*, vol. 72, no. 19, pp. 2400–2402, 05 1998. [Online]. Available: https://doi.org/10.1063/1.121368

[8] Y. Ohashi, M. Arakawa, J. Kushibiki, B. Epelbaum, and A. Winnacker, "Ultrasonic microspectroscopy characterization of AlN single crystals," *Applied Physics Express*, vol. 1, no. 7, pp. 770 041–770 043, Jul. 2008.

[9] A. Polian, M. Grimsditch, and I. Grzegory, "Elastic constants of gallium nitride," *Journal of Applied Physics*, vol. 79, no. 6, pp. 3343–3344, 03 1996. [Online]. Available: https://doi.org/10.1063/1.361236

[10] T. Deguchi, D. Ichiryu, K. Toshikawa, K. Sekiguchi, T. Sota, R. Matsuo, T. Azuhata, M. Yamaguchi, T. Yagi, S. Chichibu, and S. Nakamura, "Structural and vibrational properties of

GaN," *Journal of Applied Physics*, vol. 86, no. 4, pp. 1860–1866, 08 1999. [Online]. Available: https://doi.org/10.1063/1.370980

[11] M. Yamaguchi, T. Yagi, T. Azuhata, T. Sota, K. Suzuki, S. Chichibu, and S. Nakamura, "Brillouin scattering study of gallium nitride: elastic stiffness constants," *Journal of Physics: Condensed Matter*, vol. 9, no. 1, p. 241, jan 1997. [Online]. Available: https://dx.doi.org/10.1088/0953-8984/9/1/025

[12] Y. Takagi, M. Ahart, T. Azuhata, T. Sota, K. Suzuki, and S. Nakamura, "Brillouin scattering study in the GaN epitaxial layer," *Physica B: Condensed Matter*, vol. 219-220, pp. 547–549, 1996, pHONONS 95. [Online]. Available: https://www.sciencedirect.com/science/article/pii/0921452695008071

[13] T. Kim, J. Kim, R. Dalmau, R. Schlesser, E. Preble, and X. Jiang, "High-Temperature Electromechanical Characterization of AlN Single Crystals," *IEEE Transactions on Ultrasonics Ferroelectrics and Frequency Control*, vol. 62, pp. 1880–1887, 10 2015.

[14] L. Jin, H. Wu, Y. Zhang, Z. Qin, Y. Shi, H. Cheng, R. Zheng, and W. Chen, "The growth mode and Raman scattering characterization of m-AlN crystals grown by PVT method," *Journal of Alloys and Compounds*, vol. 824, p. 153935, 2020. [Online]. Available: https://www.sciencedirect.com/science/article/pii/S092583882030298X

[15] J. M. Hayes, M. K. Martin Kuball, Y. S. Ying Shi, and J. H. E. James H. Edgar, "Temperature Dependence of the Phonons of Bulk AlN," *Japanese Journal of Applied Physics*, vol. 39, no. 7B, p. L710, jul 2000. [Online]. Available: https://dx.doi.org/10.1143/JJAP.39.L710

[16] M. Kuball, J. M. Hayes, A. D. Prins, N. W. A. van Uden, D. J. Dunstan, Y. Shi, and J. H. Edgar, "Raman scattering studies on single-crystalline bulk AlN under high pressures," *Applied Physics Letters*, vol. 78, no. 6, pp. 724–726, 02 2001. [Online]. Available: https://doi.org/10.1063/1.1344567

[17] V. Y. Davydov, Y. E. Kitaev, I. N. Goncharuk, A. N. Smirnov, J. Graul, O. Semchinova, D. Uffmann, M. B. Smirnov, A. P. Mirgorodsky, and R. A. Evarestov, "Phonon dispersion and Raman scattering in hexagonal GaN and AlN," *Phys. Rev. B*, vol. 58, pp. 12 899–12 907, Nov 1998. [Online]. Available: https://link.aps.org/doi/10.1103/PhysRevB.58.12899

[18] U. Haboeck, H. Siegle, A. Hoffmann, and C. Thomsen, "Lattice dynamics in GaN and AlN probed with first- and second-order Raman spectroscopy," *physica status solidi (c)*, vol. n/a, no. 6, pp. 1710–1731, 2003. [Online]. Available: https://onlinelibrary.wiley.com/doi/abs/10.1002/pssc.200303130

[19] T. Kozawa, T. Kachi, H. Kano, Y. Taga, M. Hashimoto, N. Koide, and K. Manabe, "Raman scattering from LO phonon-plasmon coupled modes in gallium nitride," *Journal of Applied Physics*, vol. 75, no. 2, pp. 1098–1101, 01 1994. [Online]. Available: https://doi.org/10.1063/1.356492

[20] D. Manchon, A. Barker, P. Dean, and R. Zetterstrom, "Optical studies of the phonons and electrons in gallium nitride," *Solid State Communications*, vol. 8, no. 15, pp. 1227–1231, 1970. [Online]. Available: https://www.sciencedirect.com/science/article/pii/0038109870903650

[21] P. Perlin, C. Jauberthie-Carillon, J. P. Itie, A. San Miguel, I. Grzegory, and A. Polian, "Raman scattering and x-ray-absorption spectroscopy in gallium nitride under high pressure," *Phys. Rev. B*, vol. 45, pp. 83–89, Jan 1992. [Online]. Available: https://link.aps.org/doi/10.1103/PhysRevB.45.83

[22] G. Callsen, J. S. Reparaz, M. R. Wagner, R. Kirste, C. Nenstiel, A. Hoffmann, and M. R. Phillips, "Phonon deformation potentials in wurtzite GaN and ZnO determined by uniaxial pressure dependent Raman measurements," *Applied Physics Letters*, vol. 98, no. 6, p. 061906, 02 2011. [Online]. Available: https://doi.org/10.1063/1.3554434

[23] A. R. Goñi, H. Siegle, K. Syassen, C. Thomsen, and J.-M. Wagner, "Effect of pressure on optical phonon modes and transverse effective charges in GaN and AlN," *Phys. Rev. B*, vol. 64, p. 035205, Jun 2001. [Online]. Available: https://link.aps.org/doi/10.1103/PhysRevB.64.035205

[24] J. H. A. P. M. K. D. D. J. D. Y. S. N.W.A. Van Uden, H. Hubel and J. Edgar, "Determination of the Mode Grüneisen Parameter of AlN using different Fits on Experimental High Pressure Data," *High Pressure Research*, vol. 22, no. 1, pp. 37–41, 2002. [Online]. Available: https://doi.org/10.1080/08957950211363

[25] X. Li, L. Kong, L. Shen, J. Yang, M. Gao, T. Hu, X. Wu, and M. Li, "Synthesis and in situ high pressure Raman spectroscopy study of AlN dendritic crystal," *Materials Research Bulletin*, vol. 48, no. 9, pp. 3310–3314, 2013. [Online]. Available: https://www.sciencedirect.com/science/article/pii/S0025540813003450

[26] F. J. Manjón, D. Errandonea, N. Garro, A. H. Romero, J. Serrano, and M. Kuball, "Effect of pressure on the Raman scattering of wurtzite AlN," *physica status solidi (b)*, vol. 244, no. 1, pp. 42–47, 2007. [Online]. Available: https://onlinelibrary.wiley.com/doi/abs/10.1002/pssb.200672518

[27] H. Siegle, A. Goñi, C. Thomsen, C. Ulrich, K. Syassen, K. Schöttker, D. As, and D. Schikora, "High-Pressure Raman Scattering of Biaxially Strained GaN on GaAs," *MRS Proceedings*, vol. 468, 01 1997.

[28] I. Baghishov, J. Janssen, G. Henkelman, and D. Perez, "Application-specific machine-learned interatomic potentials: exploring the trade-off between dft convergence, mlip expressivity, and computational cost," *Digital Discovery*, vol. 5, pp. 332–347, 2026. [Online]. Available: http://dx.doi.org/10.1039/D5DD00294J

[29] D. Kuryla, F. Berger, G. Csányi, and A. Michaelides, "How accurate are dft forces? unexpectedly large uncertainties in molecular datasets," *The Journal of Chemical Physics*, vol. 163, no. 22, p. 224313, 12 2025. [Online]. Available: https://doi.org/10.1063/5.0296997